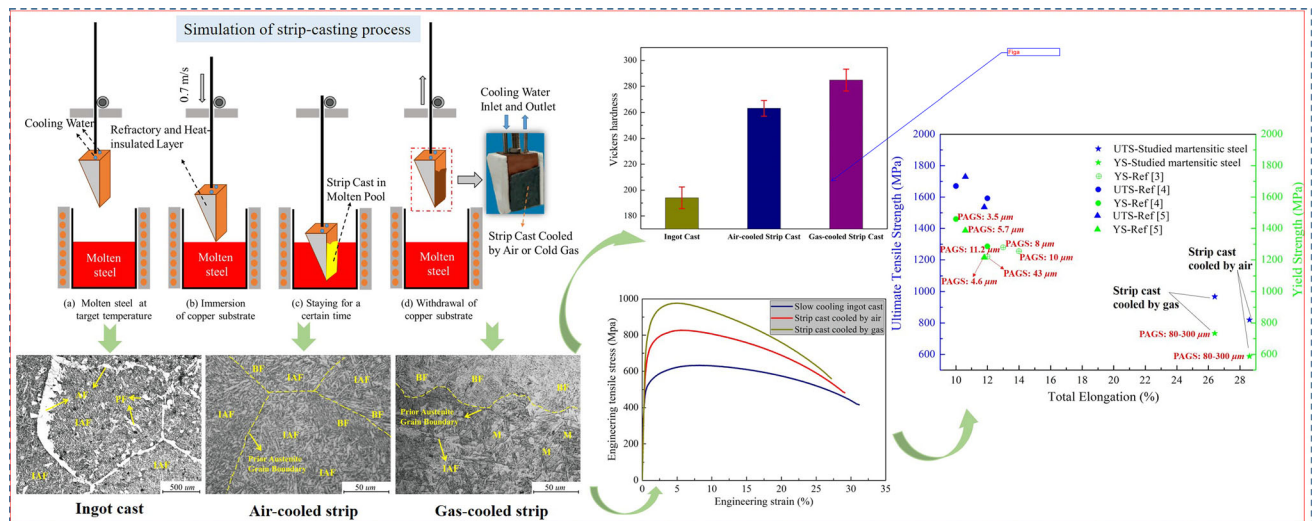


# Effect of Sub-rapid Solidification and Secondary Cooling on Microstructure and Properties of Strip Cast Low-Carbon Bainitic–Martensitic Steel



PEISHENG LYU, WANLIN WANG, CHONGHAO WANG, LEJUN ZHOU, YUAN FANG, and JIANCHUN WU

The low-carbon bainitic–martensitic steel added with microalloying elements was designed, and samples with different cooling rates were produced through ingot casting and simulated strip casting. The ingot cast presented a multiphase microstructure constituted of allotriomorphic ferrite, polygonal ferrite, acicular ferrite and pearlite. The air-cooled strip consisted of polygonal ferrite, acicular ferrite and bainite ferrite, and the gas-cooled strip was composed of acicular ferrite, bainite ferrite and martensite. The results indicated that the duplex sulfide-oxide particles were firstly formed during solidification and refined by the high solidification rate during strip casting; the embedded structure of copper sulfide in duplex particles suggested that the copper sulfide precipitated from the liquid oxide. Independent copper sulfides with an average diameter of  $\sim 80$  nm were formed in the ingot cast and a large number of nanoscale carbides or nitrides less than 25 nm was also observed. However, independent copper sulfides and nanoscale precipitates were hardly observed in the gas-cooled strip cast. For the air-cooled strip cast, only a small number of the nanoscale precipitates were observed. Vickers hardness, yield strength (YS) and ultimate tensile strength (UTS) increased with the fraction of bainite ferrite and martensite, in which the gas-cooled strip showed the highest YS and UTS, and the ingot cast presented the highest total elongation (TE). Nevertheless, the gas-cooled strip showed the best toughness due to the highest product of UTS and TE.



<https://doi.org/10.1007/s11661-021-06356-9>

© The Minerals, Metals & Materials Society and ASM International 2021

PEISHENG LYU, WANLIN WANG, and LEJUN ZHOU are with the School of Metallurgy and Environment, Central South University, Changsha, 410083, Hunan, P.R. China and also with National Center for International Research of Clean Metallurgy, Central South University, Changsha, 410083, Hunan, P.R. China. Contact e-mail: l.j.zhou@hotmail.com CHONGHAO WANG is with

the School of Metallurgy and Environment, Central South University. YUAN FANG and JIANCHUN WU are with the Research Institute, Baoshan Iron & Steel Co., Ltd., Shanghai, 201999, P.R. China. Manuscript submitted February 9, 2021; accepted June 7, 2021. Article published online June 26, 2021

## I. INTRODUCTION

DUE to the ultra-high strength that martensitic steels could achieve, they have been widely used in many industries, such as tools, constructions and automobiles.<sup>[1–3]</sup> Particularly, low-alloy low-carbon martensitic steel has a good prospect because it owns a good combination of mechanical and welding properties as well as a low production cost. At present, low-alloy low-carbon martensitic steel strips have been successfully produced through conventional hot rolling<sup>[4,5]</sup> or cold rolling<sup>[6–8]</sup> of ingot or continuous casting slab.

As an advanced near-net-shape casting technology in steel industry, strip casting can directly cast molten steel into the steel strips with several millimeters in thickness followed by in-line hot rolling or without hot rolling<sup>[9–11]</sup> Unlike conventional continuous casting and thin-slab casting, there is no mold flux covering on the molten pool during the process of strip casting, and therefore the molten steel solidifies quickly at a sub-rapid solidification rate due to the direct contact between the melt and water-cooled mold. Due to the rapid solidification of molten steel and the significant decrease of hot rolling reduction, strip casting possesses many advantages such as emission reduction, energy saving, low operating and investment costs, flexible operating system and high tolerance to impurities.<sup>[12–14]</sup> The twin-roll casting is the most mature and popular strip-casting technology for steel strip production, and it has been successfully commercialized for the production of plain carbon steel strips, microalloyed high-strength steel strips, silicon steel strips, *etc.*<sup>[10,11,15–17]</sup> However, the industrial production of low-carbon martensitic steel strips through strip-casting technology has never been reported. Due to its unique advantages, strip casting may be another potential way to produce low-carbon martensitic steel strips. Therefore, it is significant to explore the feasibility of producing low-alloy low-carbon martensitic steel by strip-casting technology.

In addition, microstructure evolution of the steel strip under the scenario of fast cooling during strip casting is an interesting topic due to its unique features that are quite different from conventional casting-rolling process, such as coarse austenite grain,<sup>[18,19]</sup> precipitation of nanoscale sulfides,<sup>[20–23]</sup> retention of Cu, Nb, O, N, S in matrix as a supersaturated solid solution,<sup>[21–25]</sup> and microsegregation of elements into the interdendritic regions.<sup>[26,27]</sup> At present, the study on the microstructure evolution and mechanical properties of low-alloy low-carbon martensitic steel produced by strip casting has been never conducted. Physical knowledge developed for the conventional casting-rolling process are not applicable to the strip-casting process. Therefore, it is necessary to make efforts to understand the microstructure characteristics of the low-alloy low-carbon martensitic steel produced by strip casting.

Strip-casting simulators have been demonstrated to be an ideal way for the fundamental studies on strip casting. For example, Xiong *et al.*<sup>[28–30]</sup> used strip-casting simulator to investigate microstructure evolution and mechanical properties of dual phase (DP) and transformation induced plasticity (TRIP) steels. Besides,

the static recrystallization of strip cast after cold rolling<sup>[31,32]</sup> and texture development during strip casting<sup>[33–35]</sup> were also studied by strip-casting simulator. In this study, the improved strip-casting simulator was developed to simulate the strip casting of low-alloy low-carbon bainitic–martensitic steel, which is named based on its final microstructure but has a similar composition to the conventional low-alloy low-carbon martensitic steel. And the steel strips under different secondary cooling conditions were obtained. Besides, the slow cooling ingot cast was prepared for comparison. Then, the effect of cooling rate including primary cooling rate (solidification rate) and secondary cooling rate on the microstructure evolution, precipitation behavior and mechanical properties of low-carbon bainitic–martensitic steel was investigated, which could provide significant guidance for the industrial production of low-carbon martensitic steel strips in the future.

## II. MATERIALS AND EXPERIMENTAL METHODS

The chemical composition of low-carbon bainitic–martensitic steel was designed based on a commercial grade of low-carbon martensitic steel, and its main composition is shown in Table I. In this study, strip cast samples were obtained by the recently developed strip-casting simulator by Steel Research Center at Central South University, China. As a physical model, the simulator can simulate the initial melt/roller contact in the actual strip caster. The detailed information of this strip-casting simulator has been discussed in the previous study.<sup>[36]</sup> It has been shown that the as-cast microstructure of the strip cast produced by a strip-casting simulator is comparable to that of the steel strip cast produced by an actual strip caster.<sup>[37]</sup> The experimental process of the simulator is shown in the Figure 1. Firstly, 5 kg experimental steel (Si–Mn deoxidized steel), was charged into the magnesia crucible and then melted by a high-frequency induction furnace to the target temperature 1560 °C. Next, the water-cooled copper substrate was immersed into the molten bath quickly and stayed for a certain time to form the strip cast with the dimension of 30 × 30 × (1.0 to 1.2) mm (Figure 2(a)). Then, the copper substrate was withdrawn from the molten bath quickly and the strip cast sample solidifying against the substrate surface was cooled by the air or by the cold gas. During the whole experimental process, the furnace chamber was protected by the ultra-high-purity argon gas. After the completion of immersion experiments, the molten steel inside magnesia crucible was cooled slowly in the argon atmosphere of the furnace chamber to form the ingot cast, and the cast samples were taken from this ingot cast for the subsequent analysis. The secondary cooling rates of the strip casts after the withdrawal of copper substrate from the molten bath were measured by a pyrometer. As shown in Figure 3, the secondary cooling rate (maximum is about 250 °C/s) of the strip cast cooled by cold gas is higher than that (maximum is about 70 °C/s) of the strip cast cooled by air. However, it should be noted

**Table I. Chemical Composition of Studied Bainitic–Martensitic Steel (Weight Percent)**

C	Si	Mn	Ti	Mo	Cu	Nb	S	O	N	Fe
0.20	0.25	1.4	0.02	0.15	0.01	0.04	< 0.003	< 0.001	< 0.005	bal.

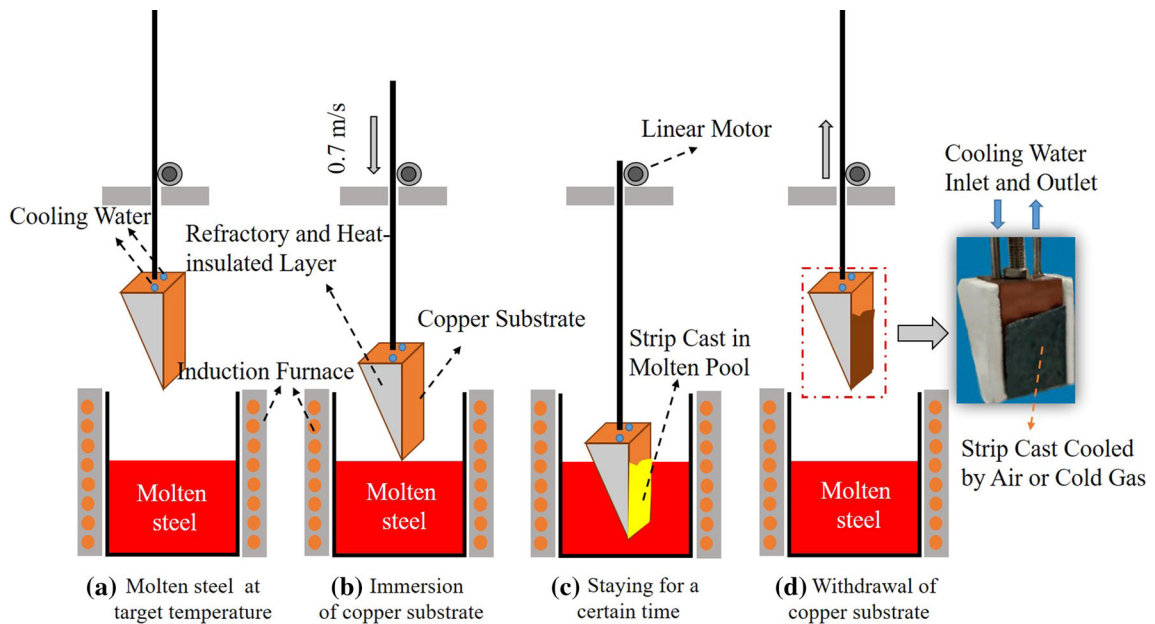


Fig. 1—Schematic diagram of the experimental process using strip-casting simulator.

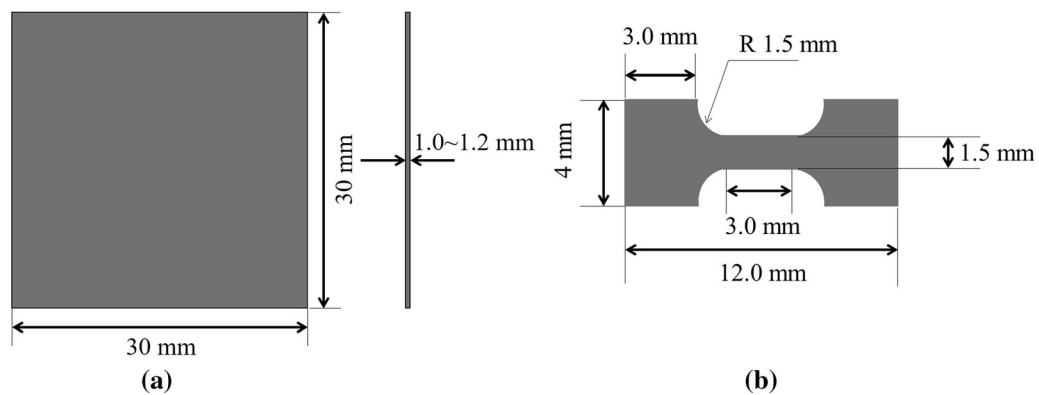


Fig. 2—Schematic diagrams of (a) strip cast sample obtained by simulator and (b) tensile test sample.

that the primary cooling rates during solidification between the two strip casts are equal to each other.

The phase component analysis of the cast sample was conducted by X-ray diffractometer (XRD, TTR III). All the cast samples including the strip and ingot casts were sectioned by wire-cutting machine and hot mounted by Struers mounting machine, and then the samples were ground and polished before further etched by 4 pct Nital. The samples were first observed by optical microscope (OM, Leica DM4000M) and scanning electron microscope (SEM, TESCAN MIRA 3 LMU) to characterize the microstructure. Subsequently, the fractions of each of phase components were calculated

based on the area fractions of different phases from SEM images using Image J, during which at least five SEM images were applied for each condition. Different phases in SEM images were outlined by Photoshop software just to make them clearer before the calculation of area fractions using Image J. The thermodynamic software (FactSage 7.1) was employed to calculate the possible precipitates of the studied samples. Meanwhile, a transmission electron microscope (TEM, JEM 2100) equipped with energy dispersive X-ray spectroscopy (EDS, Oxford X-Max20) detector was applied to analyze the microstructure and precipitation behavior of the different cast sample. For the TEM observation,

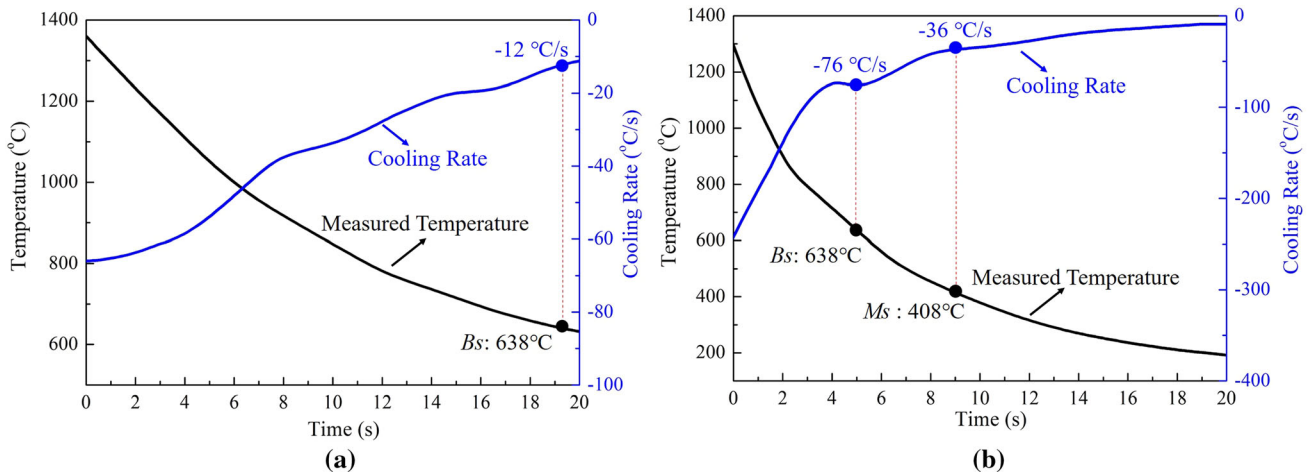


Fig. 3—Measured temperatures and cooling rates of (a) the strip cast cooled by air and (b) the strip cast cooled by cold gas after the withdrawal of copper substrate from molten steel. Note higher y-axis values in (b).

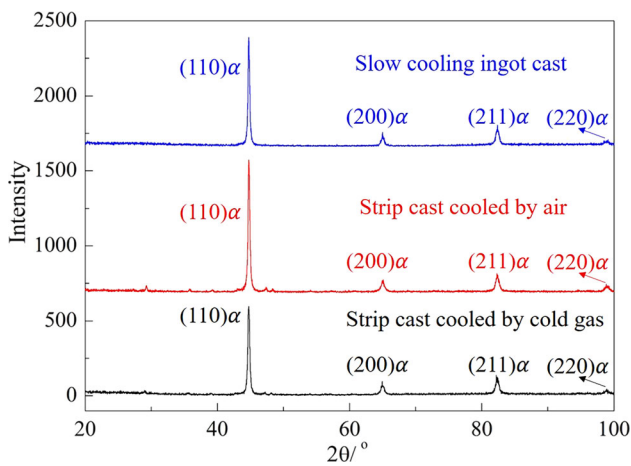


Fig. 4—X-ray diffraction patterns of cast samples obtained under different conditions.

the cast samples were firstly mechanically ground down to a thickness of 80  $\mu\text{m}$  and then polished by twin-jet electropolishing device in a solution of 10 pct perchloric acid in ethanol at the temperature lower than  $-15\text{ }^\circ\text{C}$  to obtain a thin foil. To reveal the prior austenite grain, the strip cast sample was etched by the saturated picric acid in the hot water bath and observed by confocal laser scanning microscope (CLSM, VL2000DX-SVF18SP).

For the tensile tests, all samples were manufactured to a dog-bone shape (Figure 2(b)) with a thickness between 0.8 and 1.0 mm. In this study, tensile test was conducted by material tester (MT, Z2.5TH) to measure the tensile strength and elongation of the cast samples at a dual strain rate of  $0.00025\text{ s}^{-1}$  (before necking) and  $0.008\text{ s}^{-1}$  (after necking). At least two samples were tested for each condition. After the tensile test, the fracture surface of the tensile samples was observed by scanning electron microscope (SEM, JSM-6360LV). Vickers hardness test was performed on digital Vickers hardness tester (DVHT, HVS-5) with a 3 kg load and 10 seconds retention time. More than ten repeated hardness tests

were done for each sample at different positions and the average values were taken as the final results.

### III. RESULTS

#### A. Effect of Cooling Rate on Microstructure

In this study, the microstructures of the cast samples for different cooling rate were examined. It is noted that the cooling rate includes primary cooling rate (during solidification) and secondary cooling rate (after the completion of solidification). Both of the primary and secondary cooling rate of the strip casts (cooled by air and cold gas) are far higher than that of the ingot cast treated with furnace cooling. As shown in Figure 4, the X-ray diffraction pattern indicates that the crystal structures of ingot and strip casts are body-centered cubic (BCC). It is well known that the ferrite, bainite and martensite all belong to the BCC phase components of steel material. Then, the OM, SEM and TEM were used to clarify the phase components of the ingot and strip casts. Figure 5 shows the microstructure of the slow cooling ingot cast (with low primary and secondary cooling rate), where the sample mainly consists of allotriomorphic ferrite (AF), polygonal ferrite (PF), intragranular acicular ferrite (IAF) and pearlite (P), and the coarse prior austenite grain size (PAGS) is larger than  $1000\text{ }\mu\text{m}$ , which is delineated by AF (Figure 5(a)). It can be estimated that the fractions of AF+PF and IAF+P in the ingot cast are 0.17 and 0.83, respectively.

As shown in Figures 6(a) through (d) and 7(a) through (d), the strip cast cooled by air mainly consists of polygonal ferrite (PF), intragranular acicular ferrite (IAF) and bainite ferrite (BF), and the strip cast cooled by cold gas is composed of intragranular acicular ferrite (IAF), bainite ferrite (BF) and martensite (M). It can be found from Figure 7(e) that the martensite in gas-cooled strip cast belongs to lath martensite. According to the microstructures of strip cast samples captured by SEM, it can be estimated that the fractions of PF, IAF and BF in the air-cooled strip cast are 0.08, 0.70 and 0.22,

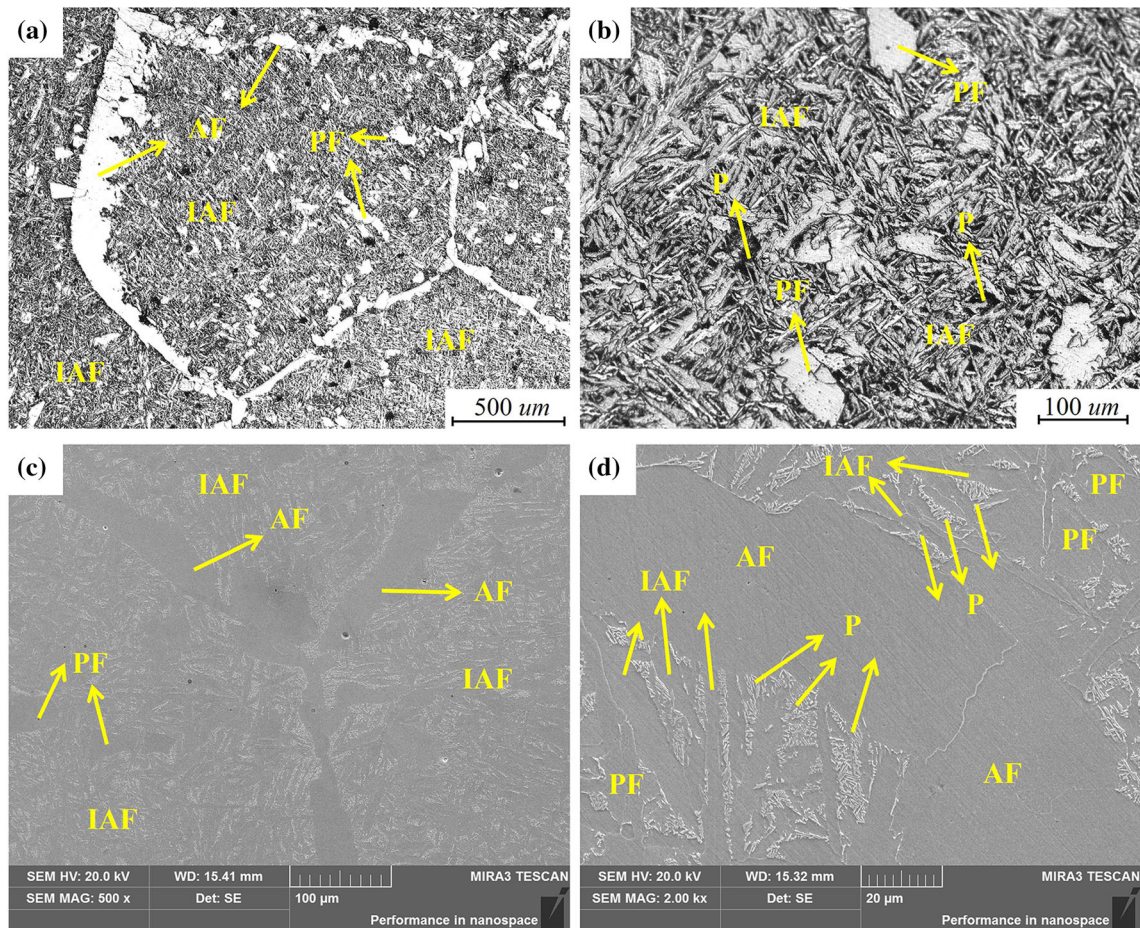


Fig. 5—(a) and (b) Optical and (c) and (d) SEM images of slow cooling ingot cast. *AF* is allotriomorphic ferrite, *PF* is polygonal ferrite, *IAF* is intragranular acicular ferrite and *P* is pearlite.

respectively, and the fractions of *IAF*, *BF* and *M* in the gas-cooled strip cast are 0.20, 0.48 and 0.32, respectively. The gas-cooled strip cast sample (Figure 6(e)) exhibits a higher dislocation density than the air-cooled strip cast (Figure 7(f)) due to the formation of martensite in gas-cooled strip cast caused by a higher secondary cooling rate. The prior austenite grain of the air-cooled strip cast was revealed by saturated picric acid and its CLSM image is shown in Figure 6(f), in which the *PAGS* is in the range of 80 to 300  $\mu\text{m}$ . Obviously, it can be found that the final microstructure and prior austenite grain of the strip cast samples get refined compared with the slow cooling ingot cast.

### B. Precipitation of Copper Sulfide and Nanoscale Particles

In this study, the inclusions larger than 1  $\mu\text{m}$  in size are not the second phase particles of interest, as some of them already existed before the solidification of molten steel, which was hardly influenced by the casting method, and others precipitated during slow solidification process of the slow cooling ingot cast. First, Factsage software was used to calculate the precipitation thermodynamics of the second phase particles in the

studied steel, as shown in Figure 8. It is suggested that under equilibrium condition the main precipitates in the studied steel after the solidification of molten steel are *MX*-type carbides and nitrides (*M* represents metal elements and *X* represents *C* or *N*). Next, TEM combined with EDS analysis was applied to study the actual precipitates of different cast samples. Copper sulfide with an average diameter of  $\sim 80$  nm can be observed in the slow cooling ingot cast according to bright-field TEM image and EDS analysis as shown in Figures 9(a) through (d). It is known that  $\text{Cu}_2\text{S}$ ,  $\text{Cu}_{1.8}\text{S}$  have a face-centered cubic (FCC) structure, and  $\text{CuS}$  has a close-packed hexagonal (HCP) structure.<sup>[38]</sup> According to the high-resolution TEM image of copper sulfide and the corresponding electron diffraction pattern (Figure 9(e)), it is indicated that the copper sulfide in the studied steel is  $\text{CuS}$  with HCP structure. It is also consistent with the EDS analysis of point A that the stoichiometric ratio between *Cu* and *S* is close to 1:1 (Figure 9(b)). Finer nanoscale precipitates with high number density were also found in the slow cooling ingot cast besides the copper sulfide, and shown in Figure 10. These nanoscale precipitates mainly present globular or rod-like morphology, and their size ( $< 25$  nm) is smaller than that of the copper sulfide. Based on

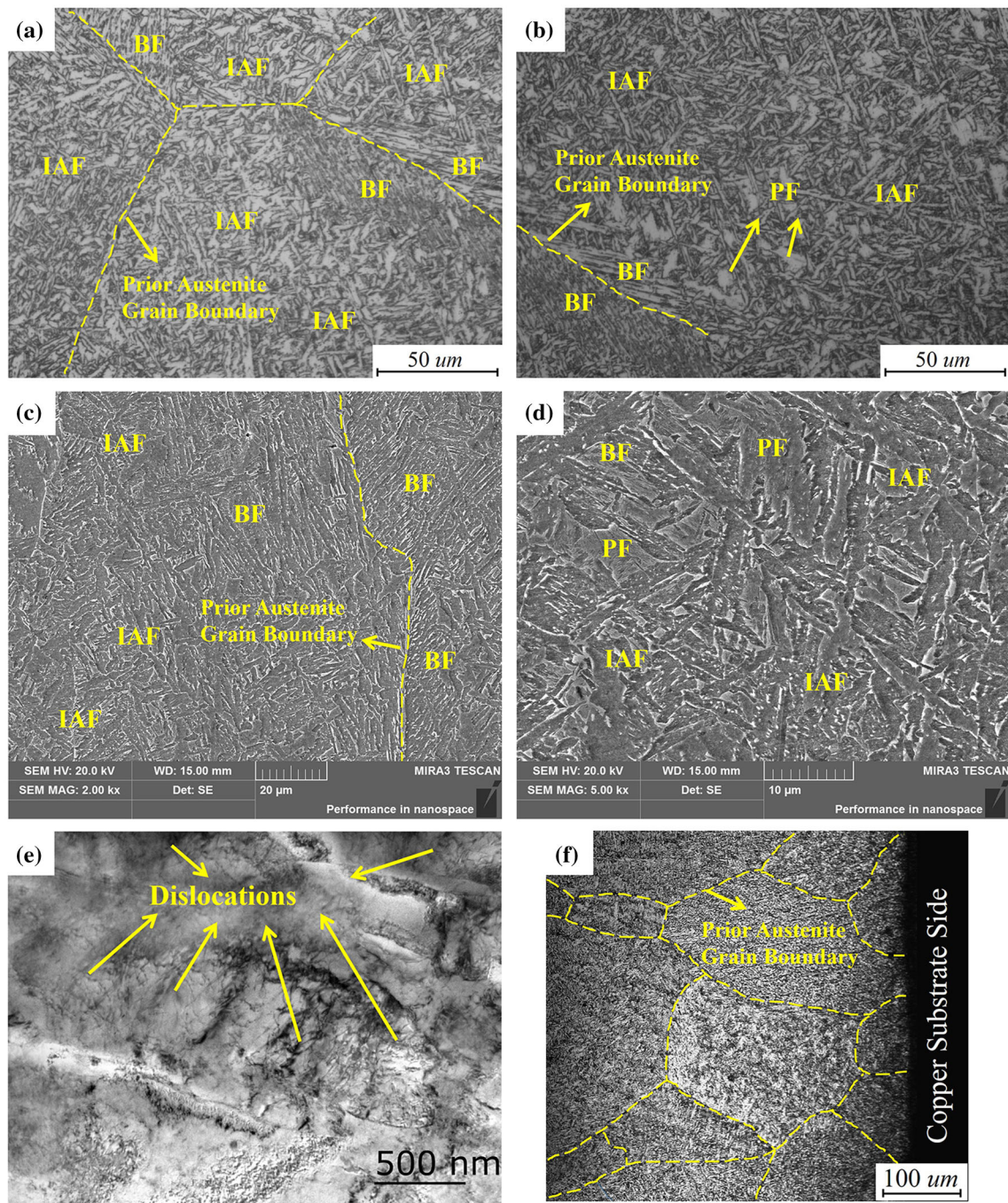


Fig. 6—(a) and (b) Optical, (c) and (d) SEM, (e) TEM and (f) CLSM images showing the microstructures of strip cast cooled by air. *PF* is polygonal ferrite, *IAF* is intragranular acicular ferrite, *BF* is bainite ferrite.

the thermodynamics analysis (Figure 8), the nanoscale precipitates can be supposed to be carbides or nitrides.

For the strip cast cooled by air, duplex sulfide-oxide particle can be observed and its diameter is about 260 nm (Figures 11(a) and (b)), in which the copper sulfide presents a globular shape (diameter ~ 185 nm) and is embedded in oxide particle. According to the EDS chemical map in Figure 11(b), it is suggested that the oxide in duplex particle is manganese silicate

( $\text{MnO}\cdot\text{SiO}_2$ ), which has a low melting point ( $< 1350^\circ\text{C}$ ).<sup>[39]</sup> Duplex sulfide-oxide particle (diameter ~ 350 nm), with a similar size and embedded structure as the air-cooled strip cast, was also found in the strip cast cooled by cold gas (Figure 11(c) and (d)). As shown in Figure 11(d), the diameter of the copper sulfide embedded in oxide particle for gas-cooled strip cast is about 210 nm. Based on the observation of a large amount of duplex sulfide-oxide particles, it seems that the size of

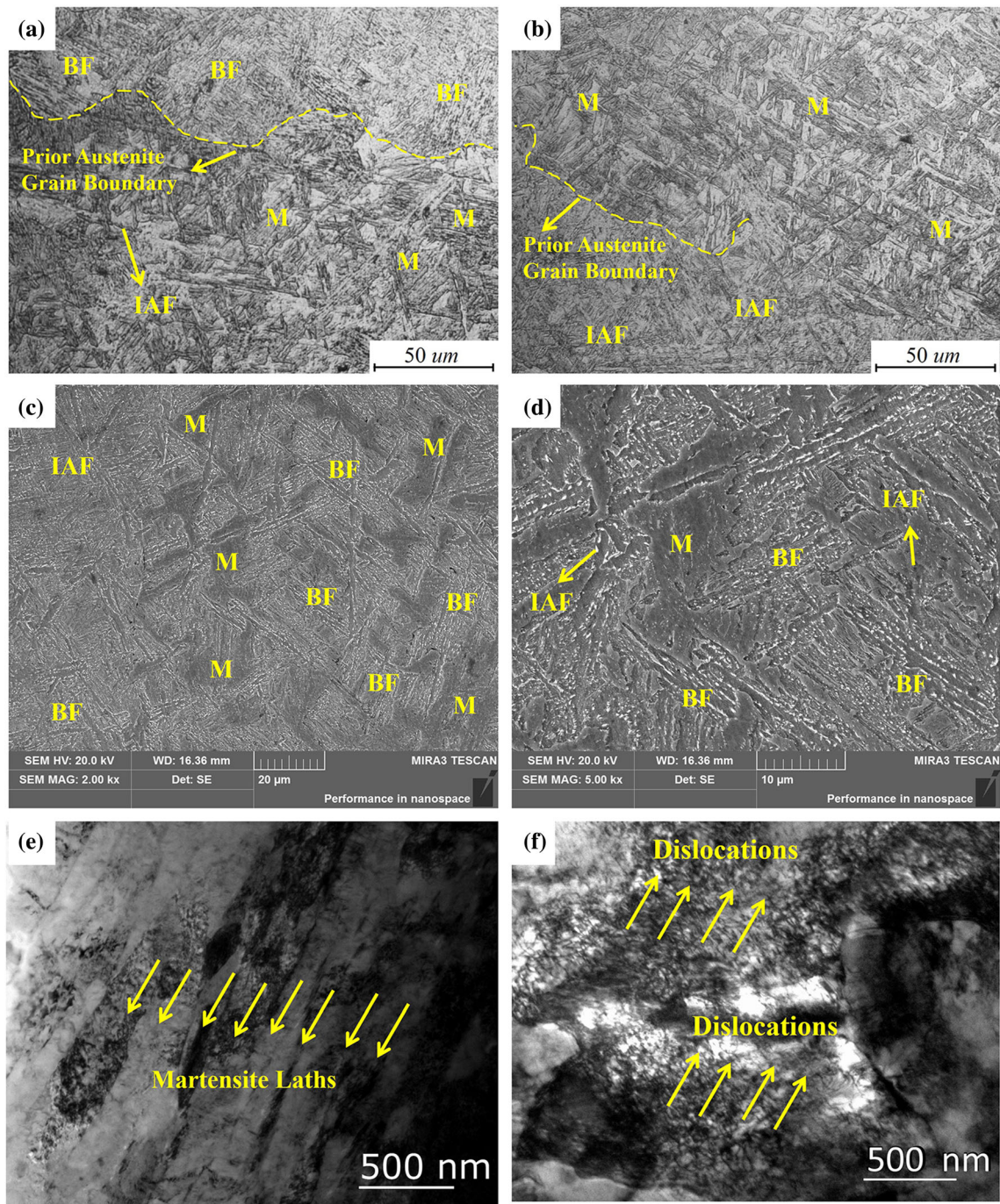


Fig. 7—(a) and (b) Optical, (c) and (d) SEM, and (e) and (f) TEM images showing the microstructures of strip cast cooled by cold gas. *IAF* is intragranular acicular ferrite, *BF* is bainite ferrite and *M* is martensite.

the duplex particle has little correlation with the second cooling rate during strip casting, and the size of the copper sulfide embedded in the oxide particle increased with the size of duplex particle. The duplex sulfide-oxide particle in low-carbon steel strip produced by pilot twin-roll caster was also reported by Liu.<sup>[38]</sup> Unlike the strip cast samples, it is noted that the duplex sulfide-oxide particles less than 1  $\mu\text{m}$  were not observed in the slow cooling ingot cast. In addition to the duplex sulfide-oxide particle, nanoscale precipitates ( $< 25 \text{ nm}$  in

size) were also found in the strip cast cooled by air, which mainly present an angular morphology (Figure 12(a)). Compared with the slow cooling ingot cast, the number density of the nanoscale precipitates is much lower in the strip cast cooled by air. However, the nanoscale precipitates were hardly observed in the strip cast cooled by cold gas, which shows an evidence that the precipitation of carbides and nitrides were suppressed and the corresponding elements were retained in

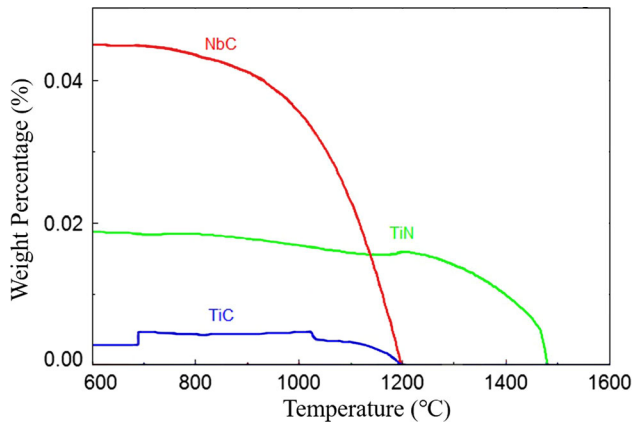


Fig. 8—Thermodynamic calculation of the precipitated second phase in the studied steel sample by Factsage software.

the matrix as a supersaturated solid solution (Figure 12(b)).

### C. Mechanical Properties

Vickers hardness of the cast samples obtained under different conditions were measured and shown in Figure 13(a). The Vickers hardness of ingot cast, air-cooled strip cast and gas-cooled strip cast were  $194 \pm 8$ ,  $263 \pm 6$  and  $285 \pm 8$ , respectively. It can be found that the hardness of the strip casts was far higher than that of the ingot cast. Figure 13(b) shows the engineering stress–strain curves of above samples, and the corresponding mechanical properties acquired from the stress–strain curves are listed in Table II. Continuous yielding phenomenon was observed for all tensile tests, which is one of the characteristics of multiphase microstructure. The reproducibility of stress–strain curves is good as demonstrated by the reasonable standard deviations in Table II. Among the three cast samples, the strip cast cooled by cold gas presents the highest yield strength (YS, 742 MPa) and ultimate tensile strength (UTS, 968 MPa), and the slow cooling ingot cast shows the highest total elongation (TE, 29.3 pct). The TE (28.6 pct) of the strip cast cooled by air is quite close to that of the slow cooling ingot cast, but its YS (581 MPa) and UTS (820 MPa) are higher than ingot cast. The strip cooled by gas shows a good combination of strength and ductility, because the product of its UTS and TE is highest (25555 MPa pct) compared with other two samples.

### D. Fractography

Figure 14 shows the representative macroscopic and microscopic SEM images of the fracture surfaces for above samples. Necking behavior can be seen from the macroscopic images (Figures 14(a1) to (c1)) for all cast samples, indicating that the ductile fracture was the dominant fracture mode, but it varied with casting condition or cooling rate. With the increasing of cooling rate, the fracture surface at low magnification changes from conical to uneven and to flat morphology; at the

same time, the fracture surface at high magnification presents smaller and shallower voids. In addition, the amount of cleavage facets on fracture surface also increases with the increasing of cooling rate. Above phenomena indicate that the ductility of cast samples reduces with the increasing of cooling rate, which is consistent with the decrement of total elongation shown in Table II.

## IV. DISCUSSION

### A. Microstructure Evolution and Precipitation Mechanism Under Different Casting Conditions

The start temperatures of bainite and martensite transformation can be estimated on the basis of the chemical composition of steel. The start temperature of bainite transformation,  $B_s$ , can be predicted by the Eq. [1] proposed by Steven and Haynes [40]:

$$B_s(^{\circ}\text{C}) = 830 - 270 \times \text{C pct} - 90 \times \text{Mn pct} - 37 \times \text{Ni pct} - 70 \times \text{Cr pct} - 83 \times \text{Mo pct} \quad [1]$$

The start temperature of martensite transformation,  $M_s$ , can be predicted by the Eq. [2] proposed by Andrew [41]:

$$M_s(^{\circ}\text{C}) = 539 - 423 \times \text{C pct} - 30.4 \times \text{Mn pct} - 11 \times \text{Si pct} - 12.1 \times \text{Cr pct} - 17.7 \times \text{Ni pct} - 7 \times \text{Mo pct} \quad [2]$$

According to the chemical composition of the studied steel, the  $B_s$  and  $M_s$  are calculated to be  $638^{\circ}\text{C}$  and  $408^{\circ}\text{C}$ , respectively. Actually, IAF is a bainite-like structure and its transformation start temperature is slightly higher than that of bainite transformation. For the slow cooling ingot cast, microstructures in Figure 5 suggest that the AF was firstly formed at the prior austenite boundary, and then a small amount of PF was formed inside the prior austenite; next, a large amount of the austenite transformed into IAF; finally, the remaining austenite transformed into P.

For the air-cooled strip cast, whose secondary cooling rate is lower than that of the cold gas-cooled one, a little amount of PF (0.08) can be observed in Figures 6(b) and (d), since diffusive transformation of austenite into ferrite took place at a relatively low secondary cooling rate. Subsequently, a large amount of austenite transformed into BF and IAF at the temperature of around  $640^{\circ}\text{C}$ . As shown in Figures 6(a) through (d), the BF presents parallel appearance of ferrite laths and most of the BF prefers to nucleate at the prior austenite grain boundaries, as indicated by the yellow dotted line. It could be found that the prior austenite grain boundaries were preserved because the BF cannot cross the austenite boundaries during the non-diffusional transformation. For the cold gas-cooled one (Figure 7(a) to (d)),



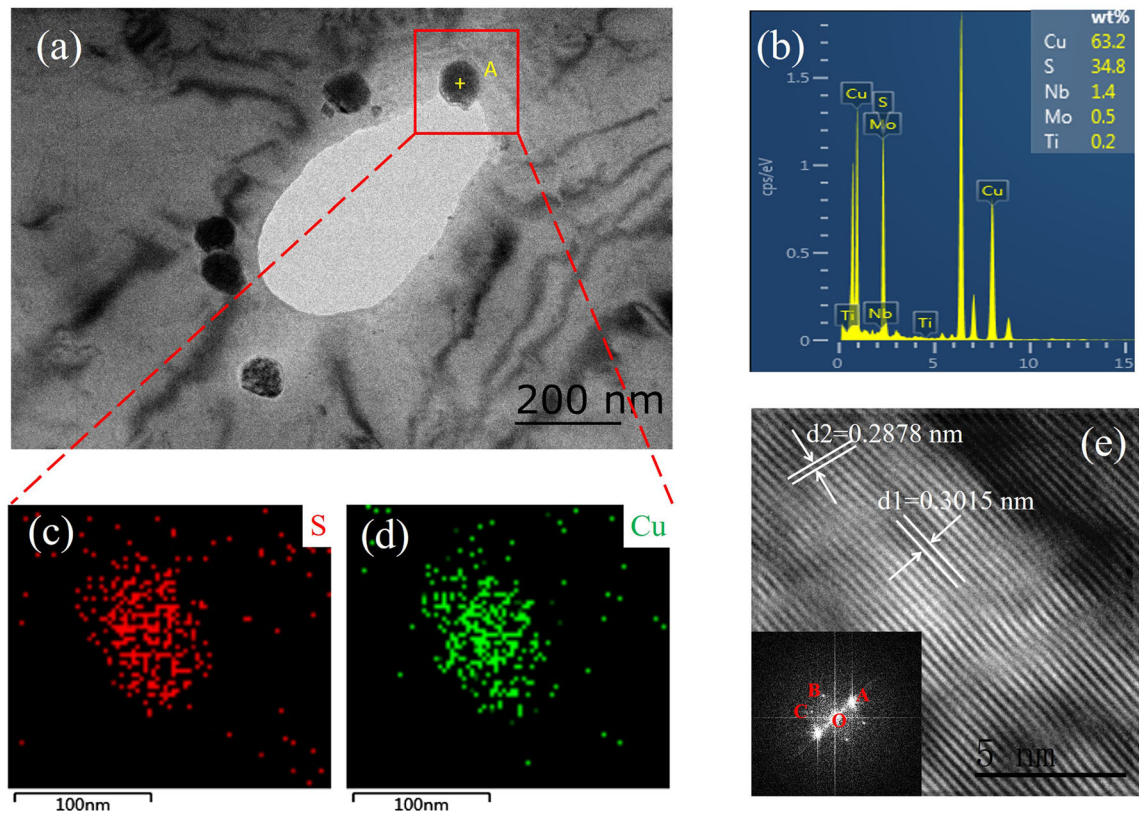


Fig. 9—Copper sulfide in slow cooling ingot cast: (a) representative bright-field TEM image, (b) EDS analysis of point A, (c) and (d) EDS chemical map of the area indicated by red box in (a), (e) high-resolution TEM image of copper sulfide and the corresponding electron diffraction pattern (Color figure online).

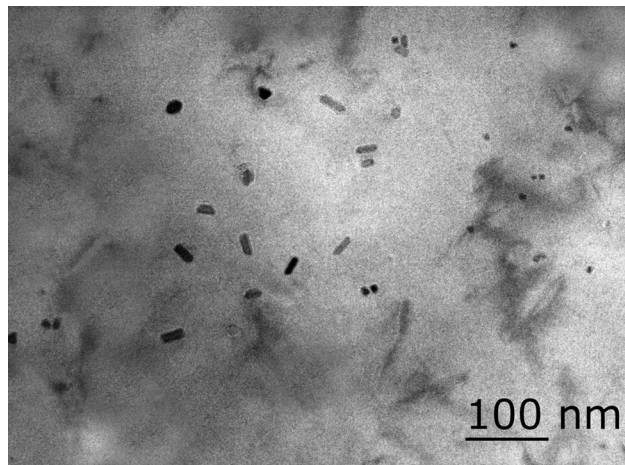


Fig. 10—TEM image showing nanoscale precipitates in slow cooling ingot cast.

the formation of PF was suppressed completely at the high secondary cooling rate, and IAF and BF were firstly formed from austenite. Then, the rest of the austenite transformed into M at the temperature of around 410 °C. All in all, the fraction of lower transformation products (BF and M) in cast samples increases with cooling rate (Table II), because the high

secondary cooling rate for the strip cast suppresses the diffusional transformation and thus results in the non-diffusional transformation of austenite into BF and M. As mentioned before, the PAGS of the strip cast produced by strip casting in this study is in the range of 80 to 300  $\mu\text{m}$  (Figure 6(f)), which is similar to those reported by others.<sup>[17–19]</sup> However, the PAGS in slow cooling ingot cast was found to be larger than 1000  $\mu\text{m}$  (Figure 5(a)). This can be attributed to the low nucleation rate during solidification at an extremely low primary cooling rate and the coarsening of austenite grain at an extremely low secondary cooling rate. Compared with the ingot cast, the smaller PAGS of the strip cast resulted in the finer microstructure (Figures 6 and 7).

As mentioned before, the small duplex sulfide-oxide particles less than 1  $\mu\text{m}$  were not observed in the slow cooling ingot cast but can be found in the strip cast (Figure 11). This is because the duplex sulfide-oxide particle was firstly formed during solidification, and its growth and coalescence was suppressed by the high primary cooling rate of the strip cast. The finding is consistent with the result reported by Suzuki<sup>[42]</sup> that the size of the inclusions formed during the solidification of molten steel decreased with the increasing of cooling rate. The size of the duplex particles found in the strip casts is similar in the two strip samples, and shows little correlation with the secondary cooling rate, although the secondary cooling rate between the air-cooled and

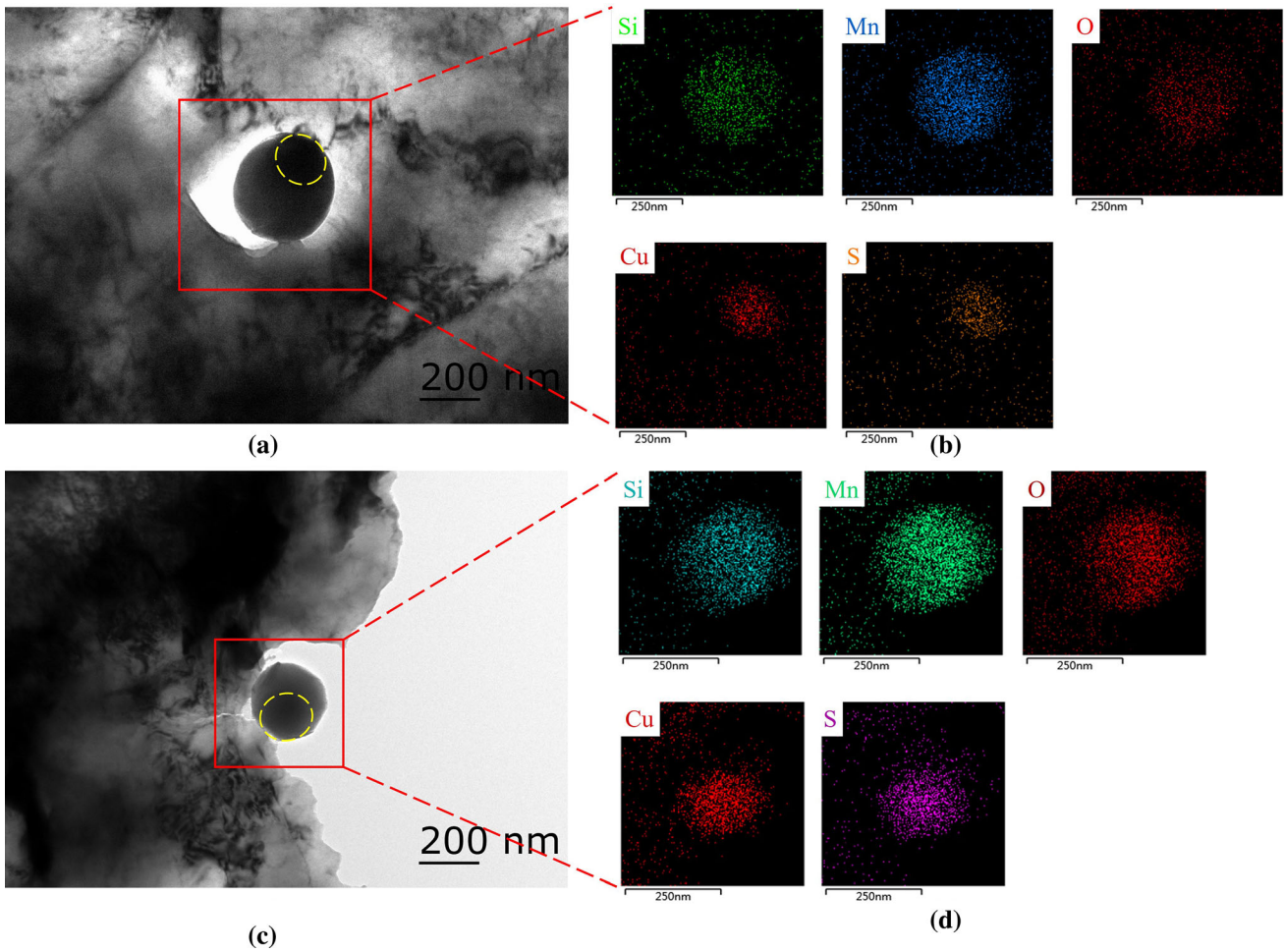


Fig. 11—(a) and (b) Typical TEM image showing duplex sulfide-oxide particle in the air-cooled strip cast and corresponding EDS chemical map. (c) and (d) Typical TEM image showing duplex sulfide-oxide particle in the gas-cooled strip cast and corresponding EDS chemical map. Yellow circle indicates copper sulfide (Color figure online).

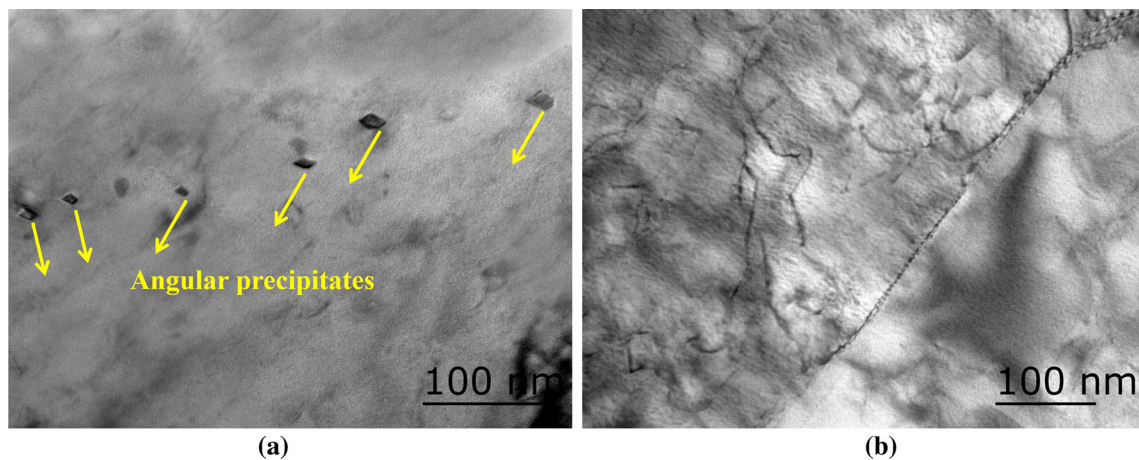


Fig. 12—Typical TEM images showing nanoscale precipitates in (a) the air-cooled strip cast and (b) the gas-cooled strip cast.

gas-cooled strip casts is different, which confirms again that the duplex particle was firstly formed during solidification.

The embedded structure of copper sulfide in duplex particle suggests that the copper sulfide precipitated from the oxide inclusion instead of the solid ferrite matrix. Consequently, the precipitation mechanism of

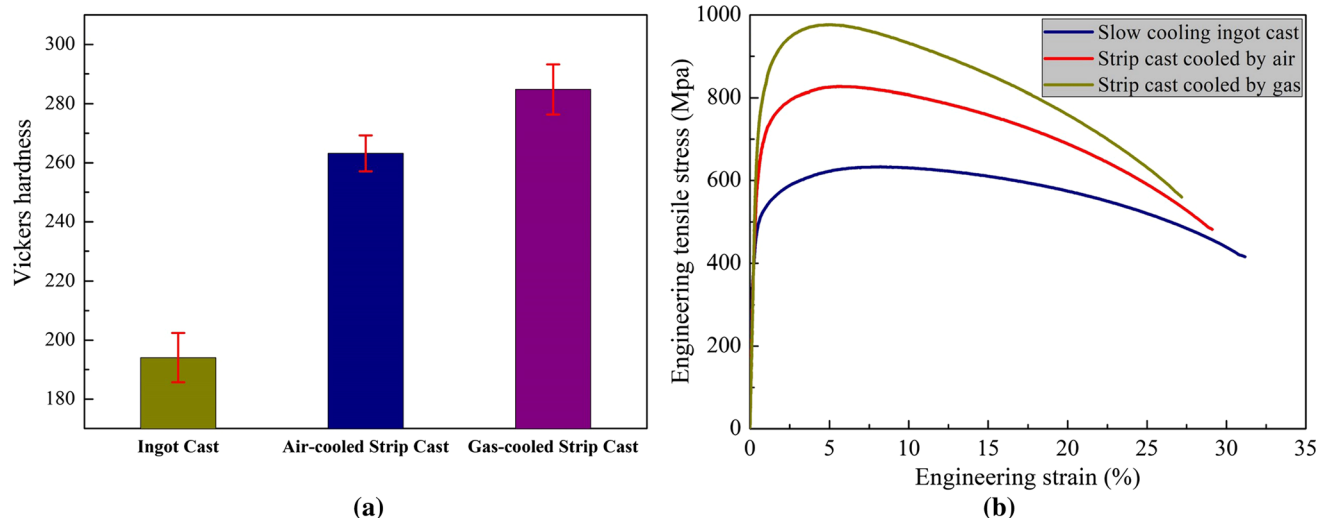


Fig. 13—(a) Vickers hardness and (b) typical engineering stress–strain curves of the samples obtained under different conditions.

duplex sulfide-oxide particle/inclusion formed during strip casting was proposed and illustrated in Figure 15. With the decreasing of temperature, the solutes elements like Si, Mn, O, Cu, S, *etc.*, would segregate into the interdendritic region around the solidification front during the solidification of strip cast (Figure 15(a)), the liquid oxide (manganese silicate) firstly precipitated from the interdendritic region due to the decreasing solubility and the enrichment of Mn, Si and O (Figure 15(b)). Meanwhile, the solutes of Cu and S would preferentially dissolve into the liquid oxide, since the sulfide has a high solubility in the silicate,<sup>[43]</sup> and they became enriched in the liquid oxide through further solidification (Figure 15(c)). Then, the oxide was enclosed by the solid matrix and still remained in the liquid state, which contained a lot of solutes of Cu and S (Figure 15(d)). With the decreasing of the liquid oxide temperature, the copper sulfide gradually precipitated from the oxide because of the decreasing solubility of Cu and S (Figure 15(e)). At last, the duplex sulfide-oxide particle was formed and the solidification process finished (Figure 15(f)).

Although the duplex sulfide-oxide particles with hundreds of nanometers in size were not found in the slow cooling ingot cast, the independent copper sulfides with an average diameter of ~ 80 nm could be found (Figure 9), which are smaller than the copper sulfide embedded in the duplex particle. This is because these independent copper sulfides precipitated from solid matrix, in which their growth was retarded due to the low diffusivity of atoms in solid condition. In addition, a high number density of nanoscale carbides or nitrides (< 25 nm in size) characterized by globular or rod-like morphology was also observed in the ingot cast (Figure 10). The reason for this could be explained as the solubility of alloying solutes in austenite or ferrite matrix decreased with the decreasing of temperature and then precipitated from solid matrix under near equilibrium condition, as shown in Figure 8.

However, the independent copper sulfides and nanoscale precipitates were hardly observed in the gas-cooled strip cast (Figure 12(b)), because the precipitation from solid matrix was suppressed due to insufficient time for precipitation to occur under fast secondary cooling rate. The independent copper sulfides also cannot be found in the air-cooled strip cast. And the number density of the nanoscale precipitates in the air-cooled strip cast (Figure 12(a)) was much lower than that of the ingot cast, indicating the incomplete precipitation under intermediate secondary cooling rate.

### B. Relationship Between Mechanical Properties and Microstructure

As shown in Figure 13 and Table II, the Vickers hardness of the cast samples obtained under different conditions increases with the increasing of YS and UTS, which is consistent with the fact that the hardness is directly proportional to the YS and UTS for the steel materials.<sup>[44]</sup> It also can be found that the Vickers hardness, YS and UTS increase with the fraction of lower transformation products (BF and M). The transformation of austenite into BF or M is achieved through displacive mechanism, and therefore the BF and M structure contain a high density of dislocations and are supersaturated with alloying elements. However, the dislocation density of M is higher than that of BF due to the lower transformation temperature of M. It is well known that there are four basic types of strengthening mechanisms for steel materials, i.e., solution strengthening, dislocation strengthening, precipitation strengthening and fine-grain strengthening.<sup>[4]</sup> Therefore, the large fraction of BF+M for both strip casts would result in the high hardness and strength due to the solution strengthening and dislocation strengthening. Compared with the ingot cast, the relatively finer final microstructure of the strip cast also contributes to the high hardness and strength by fine-grain strengthening. Despite a high number density of precipitates (Figures 9

**Table II. Mechanical Properties of Studied Low-Carbon Bainitic–Martensitic Steels**

Specimen	Fractions of Phase Components	Yield Strength (YS) (MPa)	Ultimate Tensile Strength (UTS) (MPa)	Total Elongation (TE) (Pct)	Product of UTS and TE (MPa Pct)
Slow Cooling Ingot Cast	AF + PF (0.17 ± 0.02), IAF + P (0.83 ± 0.02)	463 ± 10	644 ± 11	29.3 ± 1.8	18,869
Strip Cast Cooled by Air	PF (0.08 ± 0.02), IAF (0.70 ± 0.04), BF (0.22 ± 0.05)	581 ± 23	820 ± 14	28.6 ± 0.5	23,452
Strip Cast Cooled by Gas	IAF (0.20 ± 0.04), BF (0.48 ± 0.04), M (0.32 ± 0.02)	742 ± 24	968 ± 9	26.4 ± 0.6	25,555

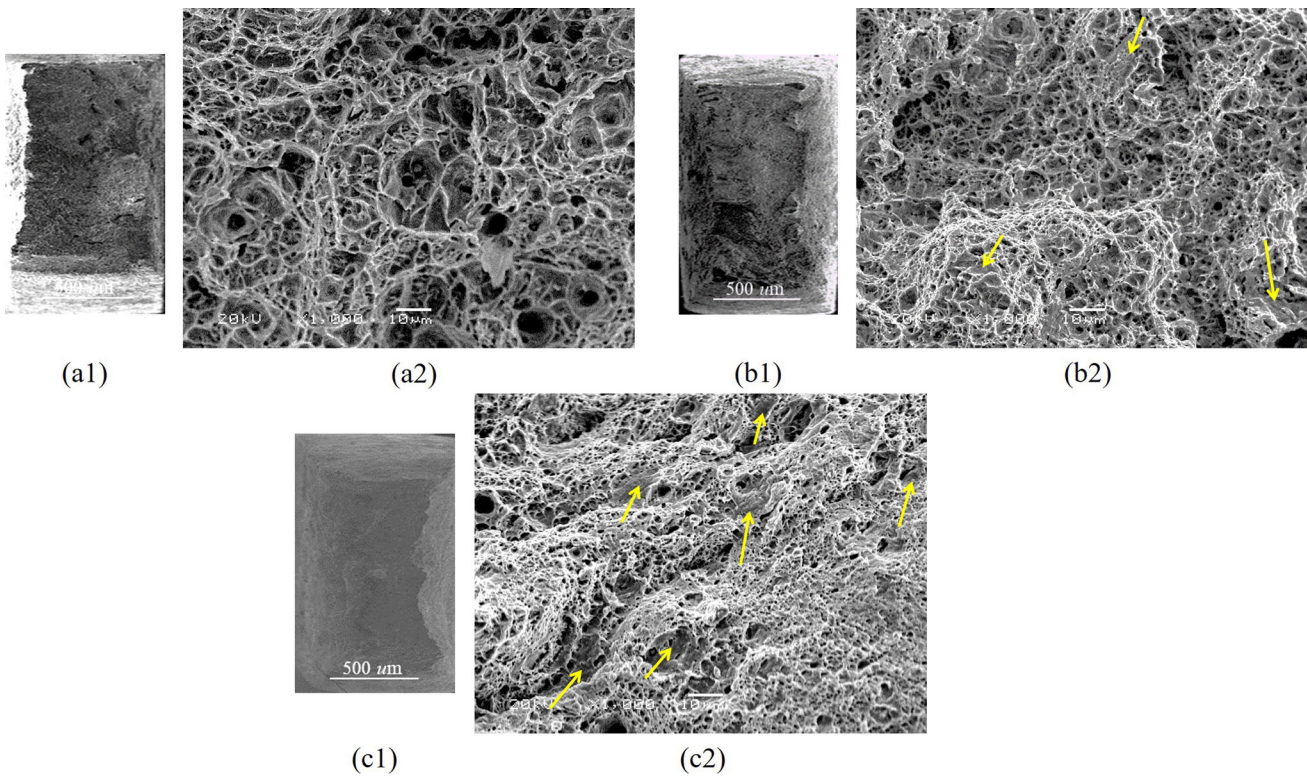


Fig. 14—Representative macroscopic (a1) through (c1) and microscopic (a2) and (c2) SEM images of fracture surfaces for (a) ingot cast, (b) strip cast cooled by air and (c) strip cast cooled by cold gas. Arrows indicate cleavage facets.

and 10) are formed in the ingot cast, the hardness and strength of the ingot cast are still far lower than that of the strip casts, suggesting that precipitation strengthening is not the dominant strengthening factor for the studied cast samples compared to the total strengthening effect of the other three strengthening mechanism. Although some nanoscale precipitates are formed in the air-cooled strip cast (Figure 12(a)) and contributes to a certain increase in strength, the hardness and strength of the gas-cooled strip cast (containing 0.48 BF and 0.32 M) are higher than that of the air-cooled strip cast (containing 0.22 BF), because the lower

transformation products dominate the strength property of the strip cast. However, ductility of the cast samples decreased with the increasing of cooling rate or fraction of BF + M as demonstrated by the reduction of total elongation (Table II) and the fractography examination (Figure 14). This is because the high density of lattice defects in BF and M hindered the movement of dislocations and thus hindered the plastic deformation, resulting in the low ductility. It is known that the product of UTS and TE can be used to characterize the toughness.<sup>[17]</sup> Although the TE of the ingot cast was highest, its toughness was lowest among the three cast

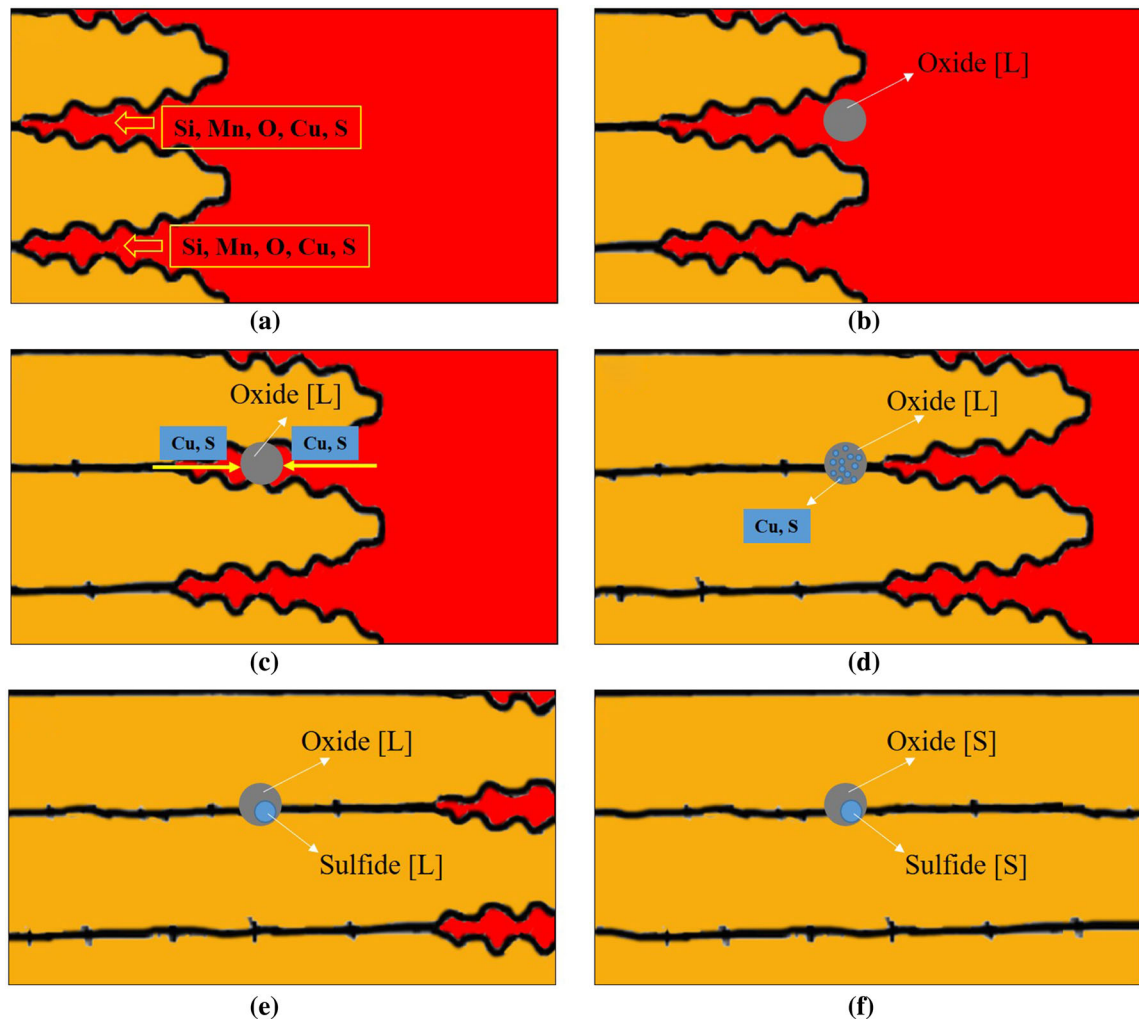


Fig. 15—Schematic illustration of precipitation mechanism of duplex sulfide-oxide particle/inclusion formed during strip casting: (a) microsegregation, (b) precipitation of liquid oxide, (c) enrichment of Cu and S elements, (d) liquid oxide enclosed by solid matrix, (e) precipitation of copper sulfide, and (f) accomplishing of solidification process. [L] represents liquid state and [S] represents solid state.

samples due to its low strength. As shown in Table II, the gas-cooled strip cast has a better toughness caused by a good combination of strength and ductility.

### C. Comparison with Tensile Properties of Hot-Rolled Low-Carbon Martensitic Steels

Figure 16 compares the tensile properties of the studied strip cast samples produced by strip casting with those of the low-carbon martensitic steels conventionally produced by hot rolling method. It can be observed that the total elongation of the strip casts in this study is higher than that of hot-rolled low-carbon martensitic steels, because the microstructure of the strip casts is not fully martensite. Compared with martensite, ferrite and bainite have a better ductility and thus have a higher elongation.<sup>[45,46]</sup> However, the UTS and YS of studied strip casts are far lower than those of hot-rolled low-carbon martensitic steels. Based on the discussion before and other references,<sup>[3–5]</sup> it is suggested that the higher strength of hot-rolled low-carbon martensitic steels is attributed to the comprehensive effect of

precipitation strengthening, fine-grain strengthening and dislocation strengthening compared to the studied strip casts. Firstly, compared with the studied strip cast samples, a higher number density of precipitates can be formed in the hot-rolled low-carbon martensitic steels,<sup>[3–5]</sup> leading to an increase in the strength of hot-rolled steel sheets by precipitation strengthening mechanism. Secondly, the strength caused by fine-grain strengthening can be calculated through the Hall–Petch equation<sup>[47]</sup>:

$$\sigma_y = \sigma_0 + kd^{-1/2} \quad [1]$$

where  $\sigma_y$  is yield strength,  $\sigma_0$  is lattice friction stress,  $k$  is Hall–Petch coefficient and  $d$  is effective grain size. As shown in Figure 16, the PAGS of hot-rolled steel sheets is much smaller than that of studied strip cast samples, which was attributed to the recrystallization during hot deformation or the phase transformation during reheating process. It has been confirmed that the small PAGS can refine the final microstructure,<sup>[48]</sup> and thus reduce the effective grain size. Based on Eq. [1], the smaller

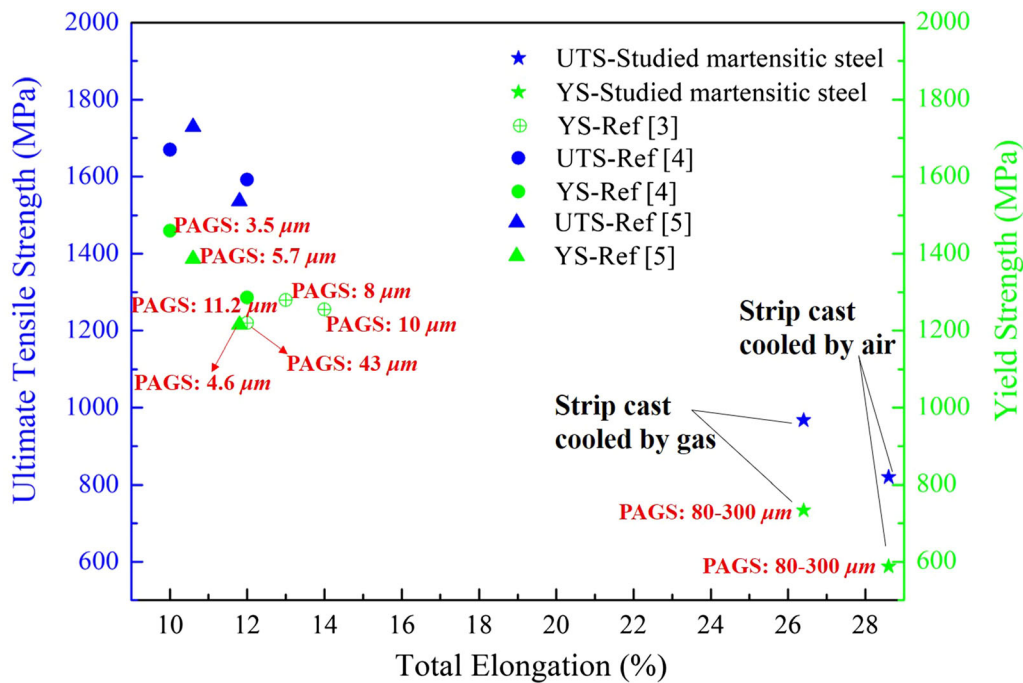


Fig. 16—Comparison of the tensile properties of the studied strip cast samples with those of the low-carbon martensitic steels conventionally produced by hot rolling method. PAGS represents prior austenite grain size for the corresponding yield strength.

effective grain size of hot-rolled steel sheets can enhance the strength of martensitic matrix by fine-grain strengthening mechanism. Thirdly, the plastic deformation in the austenite non-recrystallized region or the two-phase region during the hot rolling process resulted in an extra increment of dislocation density in the martensitic matrix of hot-rolled steel sheets,<sup>[5,49]</sup> and full martensite structure presented a higher total dislocation density compared to the partial-martensite or no-martensite microstructure of strip casts. Above two aspects can induce an increase in strength by dislocation strengthening mechanism. Although a higher total elongation of the low-carbon bainitic–martensitic strip in this study, extra measures such as hot rolling, cold rolling and proper heat treatment should be adopted during strip casting to obtain a good combination of mechanical properties.

## V. CONCLUSIONS

The strip-casting simulator has been used to simulate the strip casting of low-carbon bainitic–martensitic steel and rapidly solidified strip casts were made under different secondary cooling rate. Additionally, the slow cooling ingot cast was prepared for comparison. With the help of a range of complementary characterization techniques, the effect of cooling rate on microstructure evolution, precipitation behavior and mechanical properties of low-carbon bainitic–martensitic steel was investigated and precipitation mechanism of the duplex sulfide-oxide particle was proposed. The following conclusions have been made:

1. The ingot cast presented multiphase microstructure of AF, PF, IAF and P. However, the air-cooled strip cast consisted of PF, IAF and BF, and the gas-cooled strip cast was composed of IAF, BF, M. It is shown that high secondary cooling rate experienced during strip casting can suppress the diffusional transformation and promoted the non-diffusional transformation of austenite to BF and M.
2. The prior austenite grain size (PAGS) of the ingot cast is much larger than that of the strip casts. This can be attributed to the low nucleation rate during solidification at an extremely low primary cooling rate and the coarsening of austenite grain at an extremely low secondary cooling rate. Compared with the slow cooling ingot cast, the smaller PAGS of strip cast samples resulted in the finer final microstructure.
3. The liquid manganese silicate firstly precipitated from the interdendritic region due to the decreasing solubility and the enrichment of Mn, Si and O. Meanwhile, Cu and S in interdendritic region preferentially dissolved into the liquid oxide and became enriched in the liquid oxide through further solidification. Next, the oxide was enclosed by the solid matrix and still remained in the liquid state. With the decreasing of the liquid oxide temperature, the copper sulfide gradually precipitated from the oxide because of the decreasing solubility of Cu and S to form the duplex sulfide-oxide particle finally.
4. Independent copper sulfides were formed in the ingot cast. A high number density of finer nanoscale carbides or nitride was also observed. However, independent copper sulfides and nanoscale

precipitates were hardly observed in the gas-cooled strip cast, because the precipitation was suppressed due to insufficient time for precipitation to occur under fast secondary cooling rate. A small number of the nanoscale precipitates in the air-cooled strip cast was observed, indicating the incomplete precipitation under the intermediate secondary cooling rate.

- The gas-cooled strip cast presented the highest YS and UTS, and the ingot cast presented the highest total elongation. However, the gas-cooled strip cast showed a better toughness due to its good combination of strength and ductility compared with other two samples. The accurate quantification for grain size of final microstructure, volume of precipitate, and dislocation density is necessary in future study in order to establish the strengthening model of strip cast.

Comparison of the mechanical properties of the studied strip casts with the other low-carbon martensitic steels produced by hot rolling suggested that the higher YS and UTS of hot-rolled martensitic steels is attributed to the comprehensive effect of precipitation strengthening, fine-grain strengthening and dislocation strengthening. The accurate quantification of final grain size, volume fraction and size of precipitates, and dislocation density is necessary in future studies in order to establish the strengthening model of strip cast steel.

## ACKNOWLEDGMENTS

The financial support from National Science Foundation of China (U1760202), Hunan Scientific Technology Project (2018RS3022, 2018WK2051), and the Hunan Provincial Innovation Foundation for Post-graduate (CX20190110) are great acknowledged. The authors thank Professor Yuan Fang for the smelting of experimental steel at Baoshan Iron & Steel Co., Ltd.

## REFERENCES

- Y. Momotani, A. Shibata, D. Terada, and N. Tsuji: *Int. J. Hydrogen Energy*, 2017, vol. 42, pp. 3371–79.
- L. Xu, J. Shi, W.Q. Cao, M.Q. Wang, W.J. Hui, and H. Dong: *J. Mater. Sci.*, 2011, vol. 46, pp. 3653–58.
- L. Xu, J. Shi, W.Q. Cao, M.Q. Wang, W.J. Hui, and H. Dong: *J. Mater. Sci.*, 2011, vol. 46, pp. 6384–89.
- G.W. Yang, X.J. Sun, Z.D. Li, X.X. Li, and Q.L. Yong: *Mater. Des.*, 2013, vol. 50, pp. 102–07.
- Y. Han, J. Shi, L. Xu, W.Q. Cao, and H. Dong: *Mater. Sci. Eng. A*, 2012, vol. 553, pp. 192–99.
- M. Tokizane, N. Matsumura, K. Tsuzaki, T. Maki, and I. Tamura: *Metall. Trans. A.*, 1982, vol. 13, pp. 1379–88.
- R. Ueji, N. Tsuji, Y. Minamino, and Y. Koizumi: *Acta Mater.*, 2002, vol. 50, pp. 4177–89.
- Z.W. Liu, X.H. Guo, R.Q. Zhang, F.L. Liu, Z.H. Jin, and P.Y. Yan: *Shanghai Met. (in Chinese)*, 2017, vol. 39, pp. 27–32.
- A. Maleki, A. Taherizadeh, and N. Hosseini: *ISIJ Int.*, 2017, vol. 57, pp. 1–14.
- S. Ge, M. Isac, and R.I.L. Guthrie: *ISIJ Int.*, 2012, vol. 52, pp. 2109–22.
- N. Zapuskalov: *ISIJ Int.*, 2003, vol. 43, pp. 1115–27.
- S. Ge, M. Isac, and R.I.L. Guthrie: *ISIJ Int.*, 2013, vol. 53, pp. 729–42.
- R. Wechsler: *Scand. J. Metall.*, 2003, vol. 32, pp. 58–63.
- M. Ferry: *Direct Strip Casting of Metals and Alloys*, Woodhead Publishing, Cambridge, 2006.
- S.L. Shrestha, K.Y. Xie, C. Zhu, S.P. Ringer, C.R. Killmore, K.R. Carpenter, H.R. Kaul, J.G. Williams, and J.M. Cairney: *Mater. Sci. Eng. A*, 2013, vol. 568, pp. 88–95.
- K.Y. Xie, S.L. Shrestha, P.J. Felfel, J.M. Cairney, C.R. Killmore, K.R. Carpenter, H.R. Kaul, and S.P. Ringer: *Metall. Mater. Trans. A*, 2012, vol. 44A, pp. 848–55.
- Z.Z. Wang, K.R. Carpenter, Z.X. Chen, and C.R. Killmore: *Mater. Sci. Eng. A*, 2017, vol. 700, pp. 234–40.
- K.R. Carpenter and C.R. Killmore: *Metals*, 2015, vol. 5, pp. 1857–77.
- Z.P. Xiong, A.G. Kostyryzhev, N.E. Stanford, and E.V. Pereloma: *Mater. Des.*, 2015, vol. 88, pp. 537–49.
- Z.Z. Liu, Y. Kobayashi, and K. Nagai: *Mater. Trans.*, 2004, vol. 45, pp. 479–87.
- S. Malekjani, I.B. Timokhina, J. Wang, P.D. Hodgson, and N.E. Stanford: *Mater. Sci. Eng. A*, 2013, vol. 581, pp. 39–47.
- T. Dorin, A. Taylor, K. Wood, J. Wang, P. Hodgson, and N. Stanford: *J. Appl. Crystallogr.*, 2016, vol. 49, pp. 1777–85.
- T. Dorin, K. Wood, A. Taylor, P. Hodgson, and N. Stanford: *Mater. Charact.*, 2016, vol. 112, pp. 259–68.
- K.Y. Xie, L. Yao, C. Zhu, J.M. Cairney, C.R. Killmore, F.J. Barbaro, J.G. Williams, and S.P. Ringer: *Metall. Mater. Trans. A*, 2011, vol. 42A, pp. 2199–06.
- T. Dorin, N. Stanford, A. Taylor, and P. Hodgson: *Metall. Mater. Trans. A*, 2015, vol. 46A, pp. 5561–71.
- W.L. Wang, C.Y. Zhu, J. Zeng, C. Lu, H.R. Qian, H. Xu, and P.S. Lyu: *Metall. Mater. Trans. A*, 2020, vol. 51A, pp. 2306–17.
- W.L. Wang, C.Y. Zhu, J. Zeng, C. Lu, P.S. Lyu, H.R. Qian, and H. Xu: *Metall. Mater. Trans. B*, 2020, vol. 51B, pp. 45–53.
- Z.P. Xiong, A.A. Saleh, A.G. Kostyryzhev, and E.V. Pereloma: *J. Alloys Compd.*, 2017, vol. 721, pp. 291–306.
- Z.P. Xiong, A.G. Kostyryzhev, A.A. Saleh, L. Chen, and E.V. Pereloma: *Mater. Sci. Eng. A*, 2016, vol. 664, pp. 26–42.
- Z.P. Xiong, A.G. Kostyryzhev, L. Chen, and E.V. Pereloma: *Mater. Sci. Eng. A*, 2016, vol. 677, pp. 356–66.
- P. Sellamuthu, N. Stanford, and P.D. Hodgson: *Steel Res. Int.*, 2013, vol. 84, pp. 1273–80.
- M. Ramajayam and N. Stanford: *Mater. Sci. Eng. A*, 2016, vol. 671, pp. 147–57.
- A. Hunter and M. Ferry: *Metall. Mater. Trans. A*, 2002, vol. 33A, pp. 1499–07.
- A. Hunter and M. Ferry: *Scr. Mater.*, 2002, vol. 47, pp. 349–55.
- A. Hunter and M. Ferry: *Metall. Mater. Trans. A*, 2002, vol. 33A, pp. 3747–54.
- P.S. Lyu, W.L. Wang, H.R. Qian, J.C. Wu, and Y. Fang: *JOM*, 2020, vol. 72, pp. 1910–19.
- K. Mukunthan, L. Strezov, R. Mahapatra, and W. Blejde: *Can. Metall. Q.*, 2001, vol. 40, p. 52332.
- Z.Z. Liu, Y. Kobayashi, K. Nagai, J. Yang, and M. Kuwabara: *ISIJ Int.*, 2006, vol. 46, pp. 744–53.
- M. Wakoh, T. Sawai, and S. Mizoguchi: *ISIJ Int.*, 1996, vol. 36, pp. 1014–21.
- W. Steven and A.G. Haynes: *J. Iron Steel Inst.*, 1956, vol. 183, pp. 349–59.
- K. Andrews: *J. Iron Steel Inst.*, 1965, vol. 203, pp. 721–27.
- M. Suzuki, R. Yamaguchi, K. Murakami, and M. Nakada: *ISIJ Int.*, 2001, vol. 41, pp. 247–56.
- A. Hasegawa, K. Morita, and N. Sano: *Tetsu to Hagane (in Japanese)*, 1995, vol. 81, pp. 1109–13.
- E.J. Pavlina and C.J.V. Tyne: *J. Mater. Eng. Perform.*, 2008, vol. 17, pp. 888–93.
- A. Kumar, S.B. Singh, and K.K. Ray: *Mater. Sci. Eng. A*, 2008, vol. 474, pp. 270–82.
- N. Saeidi and A. Ekrami: *Mater. Sci. Eng. A*, 2009, vol. 523, pp. 125–29.

47. L.H. Friedman and D.C. Chrzan: *Phys. Rev. Lett.*, 1998, vol. 81, pp. 2715–18.
48. F. Wang, M.Q. Wang, J. Shi, W.J. Hui, and H. Dong: *Scr. Mater.*, 2008, vol. 58, pp. 492–95.
49. N.M. Xiao, M.M. Tong, Y.J. Lan, D.Z. Li, and Y.Y. Li: *Acta Mater.*, 2006, vol. 54, pp. 1265–78.

**Publisher's Note** Springer Nature remains neutral with regard to jurisdictional claims in published maps and institutional affiliations.